Evolution of Microstructure and Carbon Distribution During Heat Treatments of a Dual-Phase Steel: Modeling and Atom-Probe Tomography Experiments

DONG AN, SUNG-IL BAIK, SHIYAN PAN, MINGFANG ZHU, DIETER ISHEIM,
BRUCE W. KRAKAUER, and DAVID N. SEIDMAN

The temporal evolution of microstructures and carbon distributions in a Fe-0.323C-1.231Mn-0.849Si (mol pct) dual-phase steel during heat treatments are simulated using a two-dimensional cellular automaton model. The model involves austenite nucleation, phase transformations controlled by ferrite (α)/austenite (γ) interface mobility and the local carbon concentration, and long-range carbon diffusion. It is also coupled with a solute drag model to account for the effect of substitutional elements on the interface migration. The results show that after holding at 800 °C for 300 seconds the transformed γ-volume fraction is lower than the paraequilibrium prediction. During subsequent cooling at 6 °C s^{-1}, the $\gamma \rightarrow \alpha$ transformation takes place after a stagnant stage; the carbon concentrations in both the α- and γ-phases increase and become non-uniform. When cooled below 450 °C, the γ-volume fraction is nearly unchanged. A small amount of carbon enriched martensite, transformed from the remaining γ-phase, exists in the room temperature microstructure. The simulated microstructures and carbon concentrations in martensite compare reasonably well with the experimental micrographs and atom-probe tomographic measurements. During tempering at 400 °C, martensite decomposes and the carbon concentration in the α-matrix increases. The simulation results are used to understand the mechanisms of yield strength variations after different heat treatments.

https://doi.org/10.1007/s11661-018-4975-7

I. INTRODUCTION

THE transformations between the ferrite (α) and austenite (γ) phases in steels are a widely studied topic, as understanding these transformations is of central importance for the design of modern high-strength low alloyed steels, such as dual-phase (DP) steels.[1–3] Both $\alpha \rightarrow \gamma$ and $\gamma \rightarrow \alpha$ transitions are known to be the typical partitioning phase transformations. The distribution of solute atoms, especially the interstitial element carbon, not only significantly influences the phase transformation kinetics and microstructures, but also directly impacts the mechanical properties through different strengthening mechanisms, *e.g.*, solid solution strengthening.[3]

Analytical and semi-analytical models have been proposed to describe the kinetics of the $\alpha \rightarrow \gamma$ and $\gamma \rightarrow \alpha$ transformations, and the carbon concentration profile across the moving interface.[4–9] Sietsma *et al.*[4,5] studied the mixed-mode character of the $\gamma \rightarrow \alpha$ transformation in binary Fe-C alloys. Mecozzi *et al.*[6] extended the mixed-mode model to the isothermal $\alpha \rightarrow \gamma$ transformation from an initial ferrite-pearlite microstructure at inter-critical temperatures, for Fe-C-Mn alloys under the assumption of paraequilibrium,[7] in which the redistribution of substitutional alloying elements is not considered and only the carbon chemical potentials between the parent and product phases are held equal. However, it is known that the substitutional elements, *e.g.*, manganese, have a potential drag effect on the moving α/γ interfaces due to solute segregation.[8,9] Purdy and Brechet[8] proposed a solute drag model that calculates the Gibbs energy dissipation

---

DONG AN and MINGFANG ZHU are with the Jiangsu Key Laboratory for Advanced Metallic Materials, School of Materials Science and Engineering, Southeast University, Nanjing 211189, China. Conatct e-mail: zhumf@seu.edu.cn SUNG-IL BAIK, DIETER ISHEIM, and DAVID N. SEIDMAN are with the Department of Materials Science and Engineering, Northwestern University, Evanston, IL 60208 and also with Northwestern University Center for Atom Probe Tomography (NUCAPT), Evanston, IL 60208. SHIYAN PAN is with the Jiangsu Key Laboratory for Advanced Metallic Materials, School of Materials Science and Engineering, Southeast University and also with the School of Materials Science and Engineering, Nanjing University of Science and Technology, Nanjing 210094, China. BRUCE W. KRAKAUER is with the A. O. Smith Corporation, Milwaukee, WI 53224.

Manuscript submitted June 29, 2018.

resulting from the redistribution of substitutional solute at an interface. Chen and van der Zwaag[9] proposed a Gibbs energy balance (GEB) model that involves the Gibbs energy dissipation to study the $\gamma \rightarrow \alpha$ transformation in Fe-C-M ternary alloys (where M is a substitutional alloying element). The GEB model shows better agreement with experimental data compared to the paraequilibrium model. The above analytical models can describe the transformation kinetics and carbon distribution in the γ-phase, but provides less information on the carbon distribution in the α-phase. Moreover, the analytical models are incapable of depicting the realistic microstructural evolution during phase transformations.

Tremendous experimental efforts have been made to study phase transformations and control mechanical properties of various steels.[2] In recent years, electron probe microanalysis[10,11] and atom-probe tomography (APT)[12–17] have emerged as powerful techniques for local concentration measurements. With the powerful atomic-resolution, APT enables much more accurate mapping of the interstitial elements (*e.g.*, carbon) than the previous composition measurement facilities, which provides some insights into the underlying physics of solid-state phase transformations with their complex elemental distributions. Nevertheless, at present it is still difficult to observe the evolution of microstructures and solute distributions in a relatively large region and in real-time, even with the most advanced experimental facilities.

Over recent decades, with the rapid development of computer capacities and numerical techniques, computational modeling has become an important complementary tool for investigating the mechanisms of phase transformations and filling the technical gap between data generated by analytical tools and experimental observations. Different cellular automaton (CA) and phase-field (PF) models[18–30] have been developed to simulate the microstructural evolution for different heat treatments of steels: (1) the austenization process during either continuous heating or isothermal annealing in the inter-critical region[18–22]; (2) the $\gamma \rightarrow \alpha$ transformation during continuous cooling, mostly in the inter-critical temperature range[23–26]; and (3) phase transformations during the entire annealing cycle.[27–30] For simulating γ-formation from an initial ferrite-pearlite microstructure, pearlite was considered as one effective phase with the eutectoid's carbon concentration, and austenite nucleated in pearlite or at α/α grain boundaries (GBs) or both.[19,28] Some work only considered the Fe-C binary system,[24,25] and others dealt with Fe-C-M alloys using the paraequilibrium assumption.[18,19,21–23,28–30] Recently, Zhu *et al.*[28,29] and Chen *et al.*[30] combined the PF model and the solute drag model[8] to simulate phase transformations between the α- and γ-phases involving Gibbs energy dissipation in Fe-C-Mn alloys. Regarding the CA modeling, no previous work coupling with the solute drag model has been reported so far.

Due to the computational cost, most of the above numerical models are in two-dimensions (2-D), which could handle phase transformations and solute distributions efficiently. Simulations were able to replicate the experimentally observed microstructures for different heat treatments.[18–22,28] Nevertheless, previous studies by numerical modeling focused mainly on the microstructural evolution, while the evolution of the carbon distributions in different phases were less emphasized and the simulated carbon concentrations were hardly validated with the experimentally measured data. Moreover, except for a few attempts associating the simulated phase volume fraction or grain size with mechanical properties,[19,21] limited work has so far been performed to understand the relationships between processing and property utilizing the simulated microstructures involving carbon distributions.

In this article, the 2-D CA model of our previous work[31] is improved to simulate the evolution of microstructures and carbon distributions during isothermal holding at an inter-critical temperature, continuous cooling and subsequent tempering for a Fe-0.323C-1.231Mn-0.849Si (mol pct) DP steel. The CA model is incorporated with the solute drag model[8] to take into account the effect of substitutional elements on the migration of α/γ interfaces. The comparisons of the simulation results with the experimental data, involving scanning electron microscopic (SEM) micrographs and APT analyses, are presented. The behavior of the $\gamma \rightarrow \alpha$ transformation from the inter-critical temperature to the martensite start (M_s) temperature, as well as the effect of γ-grain size on the local carbon concentrations and the kinetics of $\gamma \rightarrow \alpha$ transformation, are analyzed in detail. The simulation results are then utilized to explain the mechanisms of the experimentally observed phenomena, where a DP steel exhibits different yield strengths after different heat treatments.

II. EXPERIMENT

A. *Experimental Procedures*

A commercially produced DP steel with the chemical composition 0.07C, 0.43Si, 1.22Mn, 0.051P, 0.001S (wt pct) was investigated in the present work. Samples with the dimensions $200 \times 80 \times 1.2$ mm^3 were heat treated in a box-type furnace. The following heat treated samples were studied: (1) an 800AC sample obtained by isothermal holding at 800 °C for 5 minutes and subsequent air cooling (AC, ~6 °C s^{-1}) to room temperature; and (2) an 800AC-400T sample obtained by isothermal holding at 800 °C for 5 minutes and AC (~6 °C s^{-1}) to room temperature, and then tempering at 400 °C for 20 minutes. Additionally, an 800WQ sample was prepared by isothermal holding at 800 °C and then water-quenching (WQ).

Tensile tests were performed at a crosshead speed of 6 mm min^{-1}, using a SANS CMT5105 tensile machine for samples before and after different heat treatments. The microstructures of the polished and Nital etched specimens were observed utilizing a FEI Sirion SEM. The average α-grain sizes, volume fractions, and number densities of pearlite or martensite of different samples were measured using the ImageTool software.[32]

The carbon distributions across the heterogeneous interfaces in the air cooled and tempered samples were determined utilizing a Cameca 4000X-Si local-electrode atom-probe (LEAP) tomograph.[12,13] Nanotips for performing APT were prepared utilizing a FEI Helios dual-beam focused-ion beam microscope by targeting the region of interest.[16,17] Picosecond pulses of ultraviolet laser light (355 nm wavelength) were utilized to evaporate individual atoms at a pulse repetition rate of 250 kHz, a laser energy of 20 pJ pulse^{-1}, and an average detection rate of 0.01 ions pulse^{-1}. The specimen tip temperature was maintained at 60 K, and the gauge pressure was $< 2 \times 10^{-11}$ Torr. Data analyses were performed on the 3-D reconstructions, utilizing Cameca's IVAS 3.4.6.

B. *Experimental Results*

Figure 1 presents engineering stress–strain curves of samples before and after different heat treatments. As shown, the yield platform of the 800AC sample is shorter and less obvious than that of the as-rolled sample. After tempering at 400 °C for 20 minutes, the region of constant yield strength of the 800AC-400T sample becomes longer and more obvious. Table I displays the yield strengths of different samples. It is found that the yield strength of the 800AC sample, 318 MPa, is lower than that of the as-rolled sample, 336 MPa, while the tempered 800AC-400T sample has an increased yield strength of 385 MPa compared to the 800AC sample.

SEM micrographs of samples before and after different heat treatments are given in Figure 2. The average grain sizes of different samples are measured as ~ 6 μm and essentially identical. This is considered to be due to the fact that the investigated steel was box annealed at 700 °C for 20 hours after cold-rolling, and the stored energy produced by the rolling process was essentially released, which makes the α-recrystallization unlikely to occur during heat treatments. The microstructure of the as-rolled sample, Figure 2(a), consists of a matrix of α-grains and a small quantity of pearlite distributed at the α/α GBs. The volume fraction of pearlite is measured as ~ 0.09. Figure 2(b) is the SEM micrograph of the 800WQ sample, showing martensite with a volume fraction of ~ 0.264 distributing at the α/α GBs. According to our TEM analyses, lath structure or a high density of dislocations were observed in most of the martensitic grains, indicating that the martensite existing in the 800WQ sample is a typical lath martensite.[33] Figure 2(c) shows the SEM micrograph of the 800AC sample, where bright phase distributes at the α/α GBs and most of them have a clear interface against the α-matrix. The morphology of the bright phase is apparently different from pearlite. The TEM analyses revealed that the substructure of such second phase ranges from lath (or dense dislocations) to fine internal twins, which corresponds to the feature of lath martensite and plate martensite, respectively[33]; only a small portion of the second phase contains nonparallel carbides, which might be produced by the bainitic transformation. Thus, the bright phase in the 800AC sample is identified as a type of complicated martensite containing both lath and twins, and the volume fraction of martensite is measured as ~ 0.064. Figure 2(d) is the SEM micrograph of the 800AC-400T sample, where the second phase morphology has changed evidently due to the decomposition of martensite. It is known that during tempering at an elevated temperature, tempered martensite (TM), which is a mixture of ferrite and carbides, forms through the relaxation of the distorted bcc lattice of martensite and the precipitation of carbides.[34]

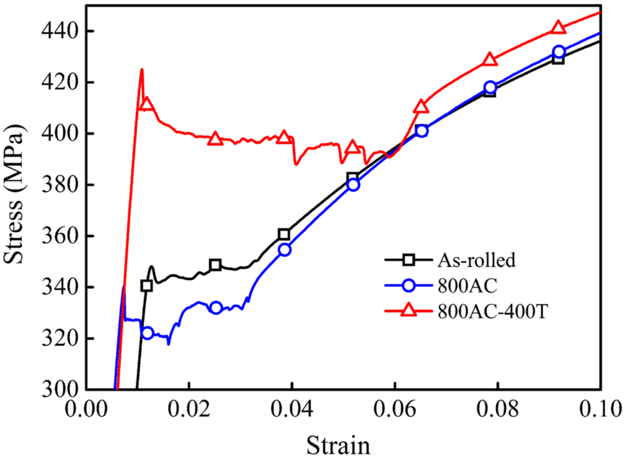

Fig. 1—Engineering stress–strain curves of samples before and after different heat treatments. 800AC: isothermal holding at 800 °C for 5 min and subsequent air cooling to room temperature; 800AC-400T: tempering the 800AC sample at 400 °C for 20 min.

APT analyses were performed on the air cooled and tempered samples. A nanotip was prepared, taken from a selected area containing an α/M interface in the 800AC sample. Figure 3(a) displays the 3-D reconstruction of solute atoms (Fe, C) in the analyzed region, where the carbon atoms are represented by black. The dark region, enriched in carbon, at the bottom-right is martensite. Figure 3(b) displays the concentration profiles of different elements, Fe, C, Mn, and Si, across the α/M interface measured by APT. As shown, the carbon concentration profile indicates a relatively high carbon concentration (~ 4 to ~ 5 mol pct) in the martensite compared to the low carbon concentration in the α-matrix (< 0.1 mol pct). The manganese profile also illustrates a relatively higher concentration in the martensite. Additionally, there is an obvious manganese spike in the interfacial region. This can be attributed to the nature of low manganese diffusivity and interfacial segregation, which may induce a solute drag effect on the migrating interface.[8,9,28–30] Regarding the silicon profile, the partitioning of silicon between the α- and γ-phases is negligible. Therefore, according to the APT measurements, the concentrations of carbon and manganese in martensite, ~ 0.97C, ~2.27 Mn (wt pct), are much higher than the nominal compositions [0.07C, 1.22Mn (wt pct)]. The continuous cooling transformation diagram indicates that for the γ-phase having such concentration levels of carbon and manganese [close to 0.97C, 2.27Mn (wt pct)], the $\gamma \rightarrow$ P transformation can be inhibited even by AC (~6 °C s^{-1}).[35] When it is cooled to the M_s temperature, the γ-phase enriched in carbon and manganese transforms to martensite.[35] Therefore, it is understandable that although the nominal carbon concentration is relatively low and the cooling rate is not fast, martensite, instead of pearlite, is observed in the 800AC sample.

Figure 4 presents the APT analysis for a nanotip taken from a selected area of the TM in a sample tempered at 400 °C for 5 minutes, which contains an interface between the α-phase and carbide. Figure 4(a) displays the 3-D reconstruction of solute atoms (Fe, C) in the analyzed region, and Figure 4(b) presents the concentration profiles for different elements (Fe, C, Mn and Si) across the heterogeneous interface; the concentration profiles were determined using the proximity histogram methodology.[36] It is noted that the carbon concentration of the carbide is close to the stoichiometry of cementite (θ), 25 mol pct. The carbon concentration of the α-phase near the cementite is measured as ~ 0.35 mol pct, using the mass spectrum analysis for the region of α-phase. We also performed analyses on other APT specimens of the same tempered sample and found that the carbon concentration of the α-phase inside TM is in the range of ~ 0.1 to ~ 0.4 mol pct, while the carbon concentration of the α-matrix outside TM is lower than ~ 0.1 mol pct. Regarding the manganese and silicon concentration profiles, the manganese partitioning to cementite is not obvious, while silicon partitions to the α-phase evidently.

It is seen from Figure 2 that the main microstructure characteristics of the samples before and after different heat treatments include α-grain size and the volume fractions of the second phases. The average α-grain sizes of the different samples are essentially identical. The volume fractions of martensite and TM in the 800AC and 800AC-400T samples are less than 0.10, which is not sufficient to make an influence on the yield strength.[37] According to the APT analyses, Figure 3, carbon and manganese are enriched in the martensite, which apparently reduces the solid solution strengthening of carbon and manganese in the α-matrix and partially explains the yield strength reduction of the 800AC sample. On the other hand, although the APT analyses in Figure 4 reveal the solute distribution inside the TM, it is insufficient to explain the yield strength increase of the 800AC-400T sample. According to the theory of Cottrell atmosphere,[38,39] the yield point is generated by the atmospheres formed around dislocations through the segregation of carbon atoms. Thus, it is considered that the different yield point phenomena of the 800AC and 800AC-400T samples should be closely related to the distribution of carbon atoms in the α-matrix. However, it is known that the minimum concentration that APT can detect is extrinsically limited by the sources of the background noise.[40] Thus, although APT can measure the carbon concentration of relatively high levels in a small region, *e.g.*, in martensite as shown in Figures 3 and 4, it is difficult using APT to accurately measure the carbon distributions in the α-matrix, where the carbon concentrations are extremely low. In addition, it is unclear that why in the 800AC sample the martensite has different morphologies and the carbon concentration of one detected region of martensite is as high as 4 to 5 mol pct.

In the following sections a 2-D CA model is presented and CA simulations are performed to study the phase transformations during different heat treatments. The CA model adopts the paraequilibrium assumption in combination with the solute drag model[8] to take into account the influence of substitutional elements on the migration of α/γ interfaces. Emphasis is placed on the evolution of carbon distributions in different phases. The CA simulations and APT analyses are then combined to interpret the different yield point phenomena of the 800AC and 800AC-400T samples shown in Figure 1.

III. GOVERNING EQUATIONS AND NUMERICAL ALGORITHMS OF THE CA MODEL

A. *Model Description*

For the sake of simplicity, the multi-component steel used in the experiment is reduced to a quaternary Fe-0.323C-1.231Mn-0.849Si (mol pct) alloy and the assumption of paraequilibrium is adopted. The Gibbs energy dissipation due to manganese diffusion inside the α/γ interface is considered through incorporating the solute drag model.[8] The effect of silicon is also involved when calculating the dissipated Gibbs energy. All thermodynamic data are obtained from the Thermo-calc® (TCFE9 database). The heat treatments used in the simulations are identical with the experiments described in Section II–A.

Since the experimentally observed α-grains are essentially equiaxed, and the measured average α-grain sizes are nearly unchanged (~ 6 μm) before and after different heat treatments (Figure 2), α-recrystallization and grain coarsening are not considered in the present model. Taking into account the balance between computational accuracy and efficiency, the grid spacing $\Delta x = 0.3\ \mu$m (except where noted) is adopted in the simulations. According to the SEM micrograph size in Figure 2, the computational domain is set as a 312 × 216 square grid. Each cell (grid unit) is characterized by several variables: (1) grain orientation, I; (2) α-phase volume fraction, φ ($\varphi = 1$ or 0 representing the α- or γ-phase, respectively); (3) mean carbon concentration, x_C, defined as $x_C = \varphi x_C^\alpha + (1-\varphi)x_C^\gamma$, where x_C^α and x_C^γ are the carbon concentrations in the α- and γ-phases, respectively; and (4) interface symbol indicating the α/α, γ/γ GBs and α/γ interfaces.

B. *Initial Microstructure and Nucleation of Austenite*

In the present work, the initial microstructure is constructed through Voronoi tessellation using the number of α-grains and pearlite volume fraction (f_P) measured from the experimental SEM micrograph, Figure 2(a). Pearlite existing in the as-rolled sample is considered as one effective phase[19,28] with the eutectoid carbon content that is determined as $x_C^{P,e} = 2.78$ mol pct utilizing Thermo-calc calculations. According to the

Table I. Yield Strengths (MPa) of the Samples Before and After Different Heat Treatments

As-rolled	Isothermal Holding at 800 °C for 5 Min Plus Air Cooling (800AC)	800AC Plus Tempering at 400 °C for 20 Min (800AC-400T)
336	318	385

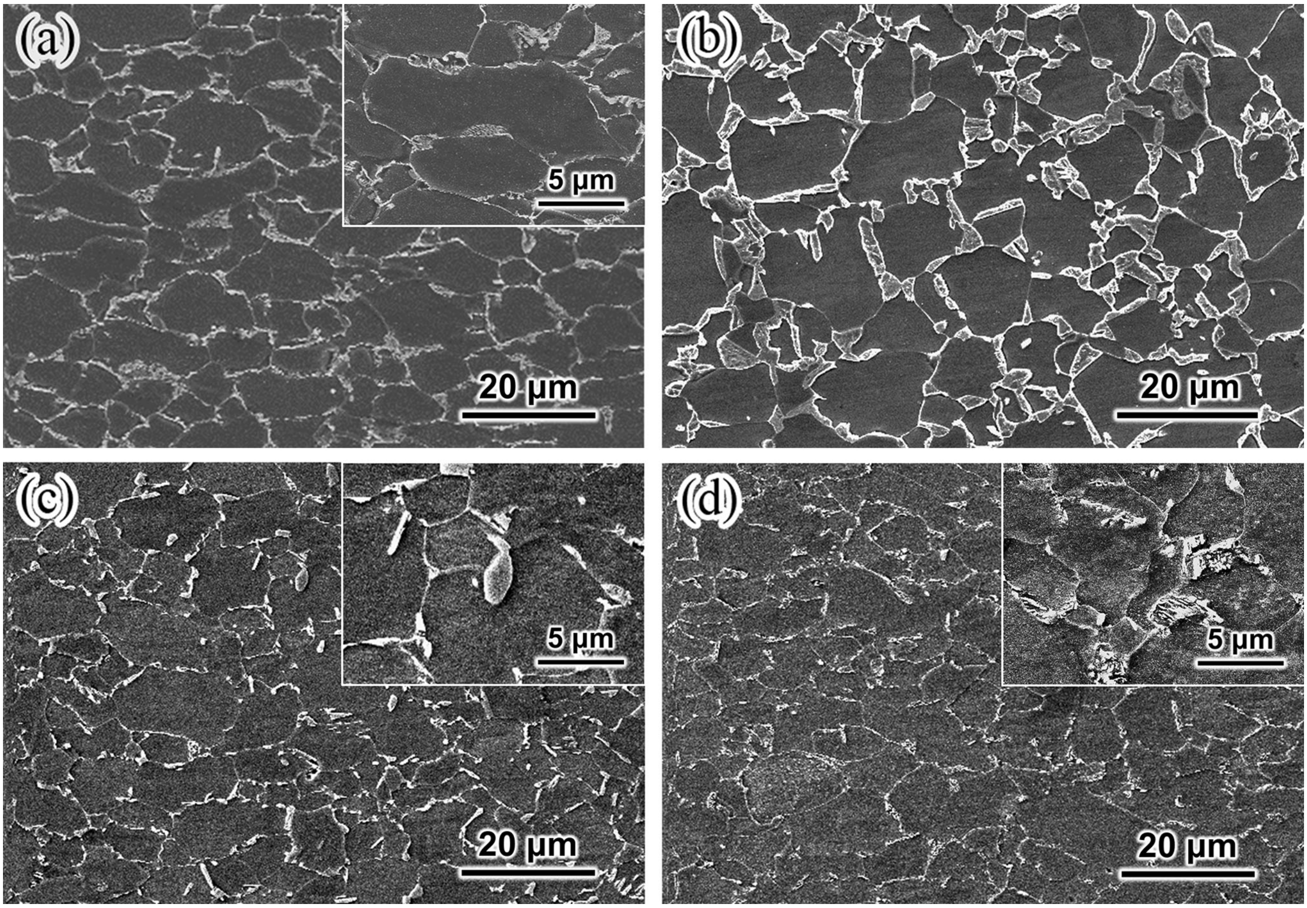

Fig. 2—SEM micrographs of samples before and after different heat treatments: (*a*) as-rolled; (*b*) holding at 800 °C for 5 min and then water-quenching (the 800WQ sample); (*c*) holding at 800 °C for 5 min followed by air cooling to room temperature (the 800AC sample); (*d*) tempering the 800AC sample at 400 °C for 20 min (the 800AC-400T sample).

experimentally measured f_P of 0.09, the initial carbon concentration of the α-phase is determined as $x_C^{\alpha,0} = 0.0792\,\mathrm{mol\,pct}$.

During inter-critical annealing, austenite formation from the initial ferrite-pearlite microstructure can be divided into two stages: (1) a rapid pearlite-to-austenite ($P \rightarrow \gamma$) transformation followed by (2) a gradual ferrite-to-austenite ($\alpha \rightarrow \gamma$) transformation.[41] As shown in Figure 2(a), the dimensions of the pearlite islands are relatively small. Thus, the initial pearlite grains are assumed to transform instantly to γ-grains with the eutectoid composition as soon as isothermal holding commences.[6] Additionally, according to our experimental observations, during isothermal holding, more γ-grains continuously nucleate preferentially at the α/α GBs. The nucleation rate of γ-grains at α/α GBs is determined using an empirical equation[21]:

$$dN/dt = K f_{\mathrm{Nuc}} N_{\mathrm{d}} A, \qquad [1]$$

where dN/dt is the γ-nucleation rate, K is an empirical factor, f_{Nuc} is the fraction of the α/α GBs without γ-nuclei, N_{d} is the γ-nucleation density, and A is the area of the computational domain. The quantities K and N_{d} are adjustable parameters and are determined by fitting the experimental data.[21,28] In the present work, the nucleation parameters are taken as $K = 0.086\ \mathrm{s}^{-1}$ and $N_{\mathrm{d}} = 8.2 \times 10^9\ \mathrm{m}^{-2}$, based on our experimental observations.

For the reverse $\gamma \rightarrow \alpha$ transformation during cooling, the nucleation of new α-grains at the γ/γ GBs are rarely observed experimentally since the γ-volume fraction (f_γ) is relatively small. The $\gamma \rightarrow \alpha$ transformation occurs primarily through reversing the migration direction of the α/γ interface with carbon redistribution, which is

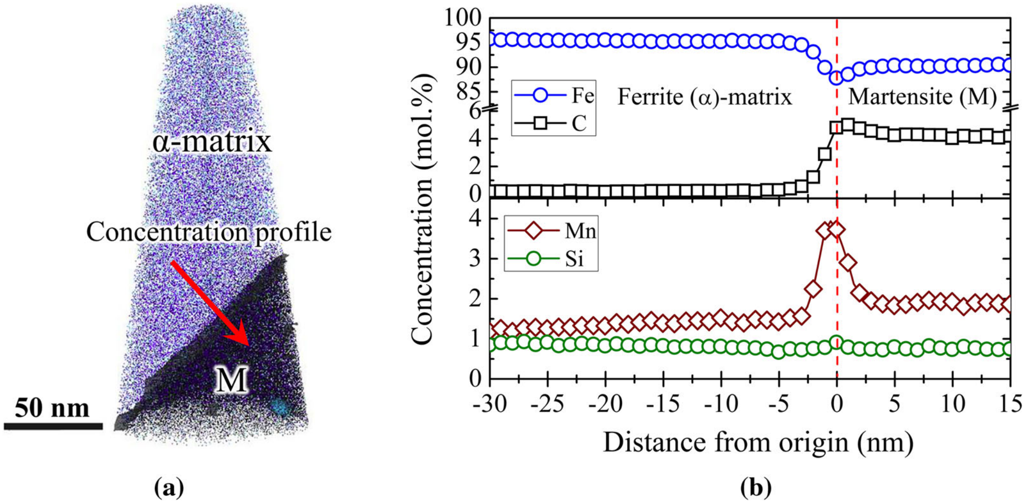

Fig. 3—APT analysis for the martensite (M) taken from the 800AC sample obtained by holding at 800 °C for 5 min followed by air cooling to room temperature: (*a*) 3-D APT reconstruction of solute atoms in the analyzed region (iron and carbon atoms are represented by blue and black, respectively); (*b*) concentration profiles for Fe, C, Mn and Si across an α-matrix/M interface (along the red arrow in (a)) (Color figure online).

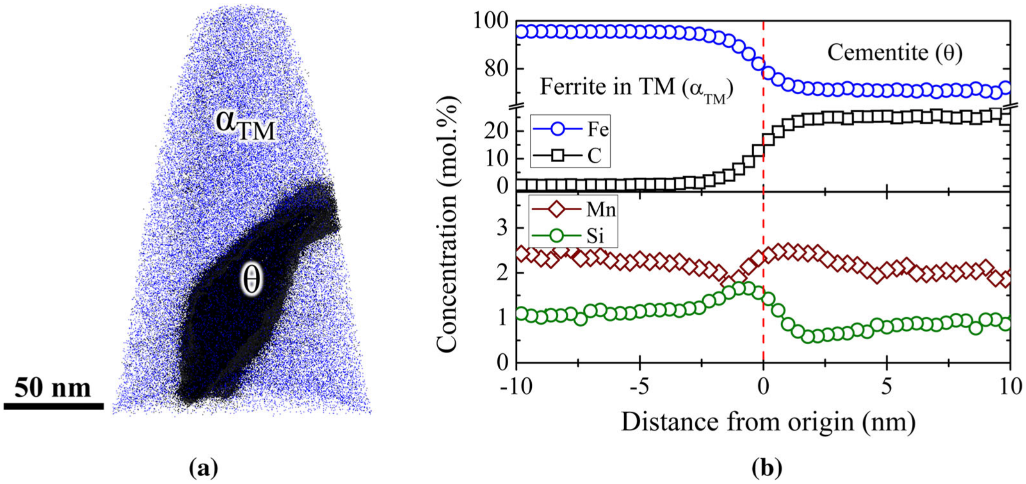

Fig. 4—APT analysis for the tempered martensite (TM) taken from the sample obtained by holding at 800 °C for 5 min followed by air cooling to room temperature and then tempering at 400 °C for 5 min: (*a*) 3-D APT reconstruction of solute atoms in the analyzed region (iron and carbon atoms are represented by blue and black, respectively); (*b*) concentration profiles for Fe, C, Mn and Si across an α_{TM}/θ interface (Color figure online).

known as the epitaxial α-growth.[42] Hence the α-nucleation during cooling is not considered in the present model.

C. *Ferrite/Austenite Interface Migration*

A mixed-mode growth model[4] is adopted to describe the α-γ transformation. The migration velocity of the α/γ interface, $v^{\alpha/\gamma}$, is calculated utilizing

$$v^{\alpha/\gamma} = M^{\alpha/\gamma}\Delta G, \qquad [2]$$

where ΔG is the effective driving pressure and $M^{\alpha/\gamma}$ is the interfacial mobility calculated from[43]

$$M^{\alpha/\gamma} = M_0^{\alpha/\gamma}\exp(-Q/RT), \qquad [3]$$

where $M_0^{\alpha/\gamma}$ is the pre-exponential factor, and Q is the activation energy taken to be 140 kJ mol^{-1}[43] for a similar alloy. The value of $M_0^{\alpha/\gamma}$ is adjustable, which depends on the alloy's composition and processing,[21,23] and it has been evaluated to be in the range of 1 × 10^{-4} to 0.5 mol m J^{-1} s^{-1}.[4–6,18–30] In the present work, $M_0^{\alpha/\gamma}$ is estimated to be 0.011 mol m J^{-1} s^{-1} based on our experimental observations.

The effective driving pressure, ΔG, involving the solute drag pressure is given by

$$\Delta G = \Delta G_{\text{chem}} - \Delta G_{\text{dis}}, \qquad [4]$$

where ΔG_{chem} is the chemical driving pressure of the α-γ transformation and ΔG_{dis} is the dissipated Gibbs energy due to the solute drag effect. ΔG_{chem} can be calculated from

$$\Delta G_{\mathrm{chem}} = \chi\left(x_{\mathrm{C}}^{\gamma,\alpha/\gamma} - x_{\mathrm{C}}^{\gamma,e}\right), \qquad [5]$$

where χ is a proportionality factor and $x_{\mathrm{C}}^{\gamma,e}$ is the paraequilibrium carbon concentration of the γ-phase, which are calculated by Thermo-calc®. The quantity $x_{\mathrm{C}}^{\gamma,\alpha/\gamma}$ is the actual carbon concentration of the γ-phase at the α/γ interface, which is obtained from the solute transport calculation, Section III–E.

According to the APT analyses of the α/γ (α/M) interface, Figure 3(a), manganese has an evident segregation at the interface. Thus, the dissipated Gibbs energy, ΔG_{dis}, is considered to be produced by the redistribution of manganese in the interfacial region, which is calculated by[8]

$$\Delta G_{\mathrm{dis}} = -\int_{-\Lambda}^{+\Lambda}\left(x_{\mathrm{Mn}}^{0} - x_{\mathrm{Mn}}(y)\right)\frac{\mathrm{d}E(y)}{\mathrm{d}y}\mathrm{d}y, \qquad [6]$$

where 2Λ is the physical interface thickness taken as 1 nm,[28–30] x_{Mn}^{0} is the bulk manganese concentration, $x_{\mathrm{Mn}}(y)$ is the manganese concentration across the interface, $E(y)$ is the interaction potential of manganese with the interface, and y is the distance from the interface. The expression of $E(y)$ is written as[8]

$$E(y) = \begin{cases} \mu_{\mathrm{Mn}}^{\alpha}, & y < -\Lambda, \\ \mu_{\mathrm{Mn}}^{\alpha} + \Delta E - E_0 + \frac{(\Delta E - E_0)}{\Lambda}y, & -\Lambda \le y < 0, \\ \mu_{\mathrm{Mn}}^{\alpha} + \Delta E - E_0 + \frac{(\Delta E + E_0)}{\Lambda}y, & 0 \le y < \Lambda, \\ \mu_{\mathrm{Mn}}^{\gamma}, & y \ge \Lambda, \end{cases}, \qquad [7]$$

where $2\Delta E$ is the potential difference of manganese between the α- and γ-phases; E_0 is the binding energy taken as $(1.4RT - 24{,}000)$ J mol^{-1},[44] where R is the gas constant and T is the temperature.

The manganese concentration profile ($x_{\mathrm{Mn}}(y)$) across the α/γ interface moving with a velocity of $v^{\alpha/\gamma}$ is given by[8]:

$$D_{\mathrm{Mn}}^{\mathrm{int}}\frac{\partial x_{\mathrm{Mn}}(y)}{\partial y} + \frac{D_{\mathrm{Mn}}^{\mathrm{int}} x_{\mathrm{Mn}}(y)}{RT}\frac{\partial E(y)}{\partial y} + v^{\alpha/\gamma}\left(x_{\mathrm{Mn}}(y) - x_{\mathrm{Mn}}^{0}\right) = 0, \qquad [8]$$

where $D_{\mathrm{Mn}}^{\mathrm{int}}$ is the diffusivity of solute manganese across the α/γ interface, taken as $1.42 \times 10^{-10}\exp(-132{,}000/RT)$ m^2 s^{-1}.[44] The parameter $2\Delta E$ is calculated with Thermo-calc® by involving the effect of silicon; E_0 and $D_{\mathrm{Mn}}^{\mathrm{int}}$ are determined using the approach given by Fazeli and Militzer[44] for a Fe-C-Mn-Si alloy.

Equations [2] through [8] can be used for the simulation of both the $\alpha \rightarrow \gamma$ and $\gamma \rightarrow \alpha$ transformations. In Eq. [5], the value of ΔG_{chem} is positive and negative for $\alpha \rightarrow \gamma$ and $\gamma \rightarrow \alpha$, respectively. A stationary interface can only start moving if the magnitude of ΔG_{chem} is greater than that of ΔG_{dis}. Otherwise the effective driving pressure ΔG is taken to be zero.[29] The incremental α-volume fraction during α-γ transformation is evaluated using:

$$\varphi = -g_{\mathrm{new}} v^{\alpha/\gamma}\Delta t/\Delta x, \qquad [9]$$

where g_{new} is a geometrical factor that is introduced to eliminate the artificial anisotropy caused by the CA square cell, and Δx and Δt are the cell size and time step, respectively. Considering that the phase transformation along GBs is faster than that in the matrix,[45] the interfacial velocity along the α/α GBs is assumed 2.5 times faster during isothermal holding. The geometrical factor, g_{new}, is related to the states of the neighboring cells and defined by

$$g_{\mathrm{new}} = \min\left[1, \frac{1}{3}\left(\sum_{m=1}^{4} S_m^{\mathrm{I}} + \frac{1}{\sqrt{2}}\sum_{m=1}^{4} S_m^{\mathrm{II}}\right)\right],$$
$$S^{\mathrm{I}},\ S^{\mathrm{II}} = \begin{cases} 0\ (f_{\mathrm{new}} < 1), \\ 1\ (f_{\mathrm{new}} = 1), \end{cases} \qquad [10]$$

where S^{I} and S^{II} indicate the states of the nearest neighbor cells and the second-nearest neighbor cells, respectively, and f_{new} is the new phase fraction of the neighboring cells.

D. *Martensite Formation and Decomposition*

As described in Section II, martensite, instead of pearlite, is observed in the 800AC sample. Thus, the $\gamma \rightarrow$ P transformation (P = pearlite) is not considered in the present model. During cooling, the $\gamma \rightarrow \alpha$ transformation takes place before reaching the M_{s} temperature. According to the martensite composition measured by APT [0.97C, 2.27Mn, 0.68Si (wt pct)] and the empirical equation proposed by Capdevila *et al.*,[46] the M_{s} temperature is estimated to be 117 °C. When cooling to the M_{s} temperature, the remaining γ-phase transforms instantaneously to martensite.

During tempering, martensite decomposes into TM, which is a mixture of ferrite and carbides.[34] In experimental studies, the Johnson–Mehl–Avrami (JMA) equation is usually adopted to describe the kinetics of martensite tempering.[47,48] Based on the JMA equation, the transformed fraction (M → TM), f, as a function of tempering time, t, can be evaluated from:

$$f = 1 - \exp[-(\beta t)^n], \qquad [11]$$

where β is a temperature dependent parameter and n is a temporal exponent. The quantities β and n are both adjustable parameters, which depend on the alloy's composition and the temperature of the tempering stage, and were usually evaluated to be from 2.69×10^{-5} to 0.368 s^{-1} for the parameter β and from 0.37 to 0.8 for the parameter n.[47,48] In the present CA simulation, β and n are taken to be 0.36 s^{-1} and 0.4, respectively.

E. *Carbon Diffusion*

In the present 2-D model, carbon partitions and diffuses according to

$$\partial x_{\mathrm{C}}/\partial t = \nabla \cdot [D_{\mathrm{C}}(\varphi) \cdot \nabla (x_{\mathrm{C}}/p(\varphi))], \qquad [12]$$

where $p(\varphi) = \varphi + k_{\mathrm{e}}(1 - \varphi)$ and k_{e} is the equilibrium partitioning coefficient determined by $k_{\mathrm{e}} = x_{\mathrm{C}}^{\gamma,e}/x_{\mathrm{C}}^{\alpha,e}$. $D_{\mathrm{C}}(\varphi)$ is the carbon diffusion coefficient associated with the α-volume fraction, and defined by $D_{\mathrm{C}}(\varphi) = \varphi D_{\mathrm{C}}^{\alpha} + k_{\mathrm{e}}(1 - \varphi)D_{\mathrm{C}}^{\gamma}$, where D_{C}^{α} [$2.2 \times 10^{-4}\exp(-122{,}500/RT(K))$ $\mathrm{m}^2\,\mathrm{s}^{-1}$] and D_{C}^{γ} [$1.5 \times 10^{-5}\exp(-142{,}100/RT(K))$ $\mathrm{m}^2\,\mathrm{s}^{-1}$] are the temperature dependent carbon diffusivities in the α- and γ-phases, respectively.[23] Equation [12] is solved using the explicit finite difference scheme and the time step is determined by $\Delta t = \Delta x^2/(4.5D_{\mathrm{C}}^{\alpha})$. The zero-flux boundary condition is applied at the four walls of the calculation domain.

IV. SIMULATION RESULTS AND DISCUSSION

A. *Model Validation*

To test the present CA model, 1-D CA simulations with and without considering Gibbs energy dissipation are performed for the $\gamma \rightarrow \alpha$ transformation during isothermal holding at the inter-critical temperature of 785 °C for a Fe-0.463C-0.506Mn (mol pct) alloy. The CA simulation results are compared with the PF simulations by Chen *et al.*[30] The used parameters, including the domain length, interfacial mobility $M^{\alpha/\gamma}$, the trans-interface diffusivity of manganese $D_{\mathrm{Mn}}^{\mathrm{int}}$ and the binding energy of manganese E_0 are identical with those adopted in the PF simulation of Chen *et al.*[30] The grid spacing is taken as 0.05 μm.

Figure 5 presents the α-volume fraction as a function of time during holding at 785 °C for 250 seconds calculated by the 1-D PF[30] and CA models. As shown, when the Gibbs energy dissipation is involved, the transformation kinetics becomes slower evidently and the final α-volume fraction is apparently lower than that without considering the Gibbs energy dissipation. This indicates that the phase transformation cannot reach the paraequilibrium state due to the solute drag pressure acting on the moving interface. The CA simulations agree reasonably well with the PF predictions[30] for both cases.

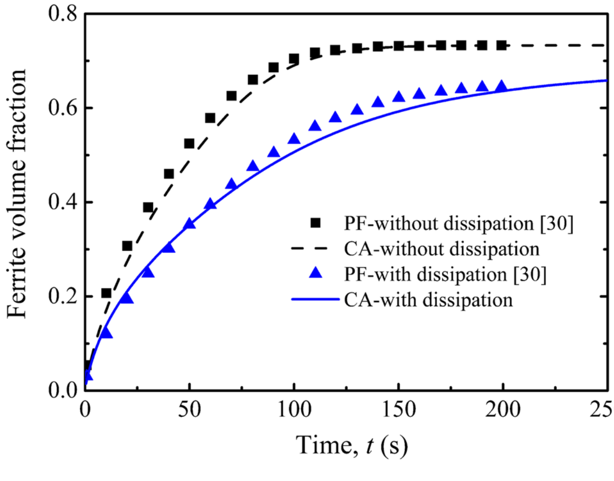

Fig. 5—A comparison of α-volume fraction as a function of time during isothermal holding at 785 °C for 250 s for a Fe-0.463C-0.506Mn (mol pct) alloy, calculated by the 1-D PF[30] and CA models.

B. *Isothermal Holding Process*

As described in Section III–B, during isothermal holding at the inter-critical temperature of 800 °C (T_{eu} = 697 °C), the pearlite transforms to the γ-phase instantaneously. Subsequently, the $\alpha \rightarrow \gamma$ phase transformation occurs, which involves the continuous nucleation of new γ-nuclei at the α/α GBs and is accompanied by carbon partitioning and diffusion. Figure 6 shows the evolution of the simulated microstructures and carbon concentration field during holding at 800 °C. The initial microstructure consists of an α-matrix with $x_{\mathrm{C}}^{\alpha,0} = 0.0792\,\mathrm{mol\,pct}$ and pearlitic grains (f_{P} = 0.09) distributed at the α/α GBs, which transform instantly to γ-grains with the eutectoid carbon content ($x_{\mathrm{C}}^{\mathrm{P,e}} = 2.78\,\mathrm{mol\,pct}$) as soon as isothermal holding commences, Figure 6(a). After holding for 3 seconds, Figure 6(b), some γ-grains have a relatively larger size and higher carbon concentrations (~ 1.841 mol pct), which are transformed from the pearlite, while some others having relatively smaller sizes and slightly lower concentrations (~ 1.750 mol pct) are apparently newly formed γ-grains. It is also observed that the carbon concentrations in the central region of the α-grains, ~ 0.0620 mol pct, are slightly greater than those in areas adjacent to small γ-grains, ~ 0.0611 mol pct, but nearly identical or even slightly lower than those close to large γ-grains, ~ 0.0628 mol pct. This indicates that γ-grains nucleated from the pearlite grow mainly by consuming the supersaturated carbon atoms in the γ-phase, while the γ-grains nucleated at the α/α GBs grow by absorbing carbon atoms from the adjacent α-phase. As a result, carbon concentration gradients are produced ahead of the α/γ interface, which drives carbon diffusion in both the α- and γ-phases. The carbon concentrations in both α- and γ-phases decrease and become uniform gradually with time, as observed in Figures 6(b) through (d). Figure 6(d) indicates that the carbon concentrations in both phases achieve their stable values ($x_{\mathrm{C}}^{\alpha} = 0.0423\,\mathrm{mol\,pct}$ and $x_{\mathrm{C}}^{\gamma} = 1.222\,\mathrm{mol\,pct}$), respectively, which are higher than the paraequilibrium values ($x_{\mathrm{C}}^{\alpha,e} = 0.0312\,\mathrm{mol\,pct}$ and $x_{\mathrm{C}}^{\gamma,e} = 0.899\,\mathrm{mol\,pct}$). The transformed γ-volume fraction (f_{γ}) calculated by the CA simulation is 0.238, which is nearly coincident with the experimental measurement (~ 0.264) of the quenched sample, Figure 2(b), but apparently lower than the paraequilibrium fraction of 0.336. This confirms that the $\alpha \rightarrow \gamma$ phase transformation does not reach the paraequilibrium state due to the Gibbs energy dissipation. The uniform carbon distribution in the γ-phase with a concentration of 1.222 mol pct (~ 0.267 wt pct) also explains the experimental observation that the martensite existing in the 800WQ sample is essentially lath martensite, which is normally formed in low- or medium-carbon steels.[33] The simulated microstructure (Figure 6(d)) agrees reasonably well with the SEM micrograph of the 800WQ sample (Figure 2(b)).

Figure 7(a) presents the simulated f_γ as a function of time during isothermal holding at 800 °C for 300 seconds. It is found that the transformation rate of $\alpha \rightarrow \gamma$ gradually decreases with time, and the f_γ approaches the stable value of 0.238 within 50 seconds. Figure 7(b) presents the average chemical driving pressure, ΔG_{chem}, and dissipation, ΔG_{dis}, as a function of time. It is noted that ΔG_{chem} has a dramatic decrease within 20 seconds,

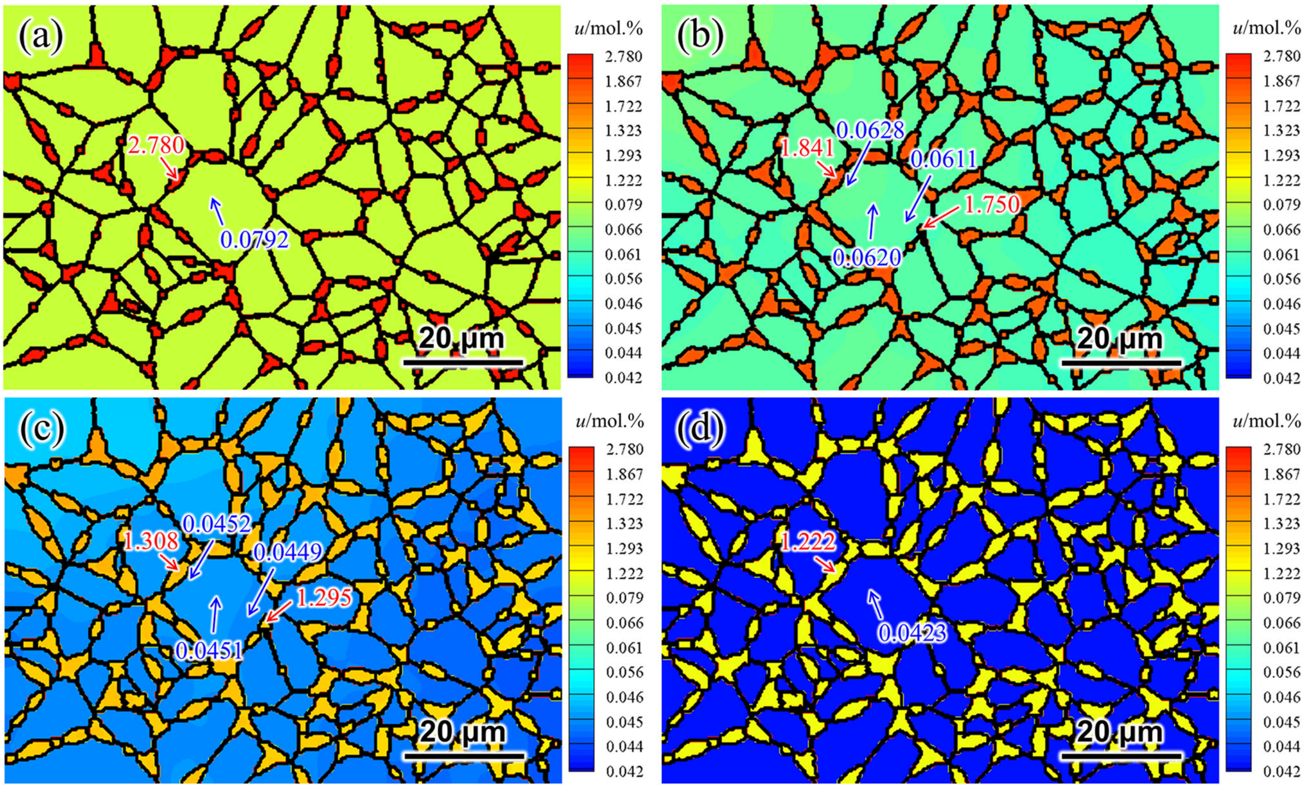

Fig. 6—Simulated microstructures and carbon concentration fields of a Fe-0.323C-1.231Mn-0.849Si (mol pct) alloy during isothermal holding at 800 °C for: (*a*) 0 s; (*b*) 3 s; (*c*) 15 s; (*d*) 300 s. The numbers in blue and red indicate the local carbon concentrations in the α- and γ-grains, respectively (Color figure online).

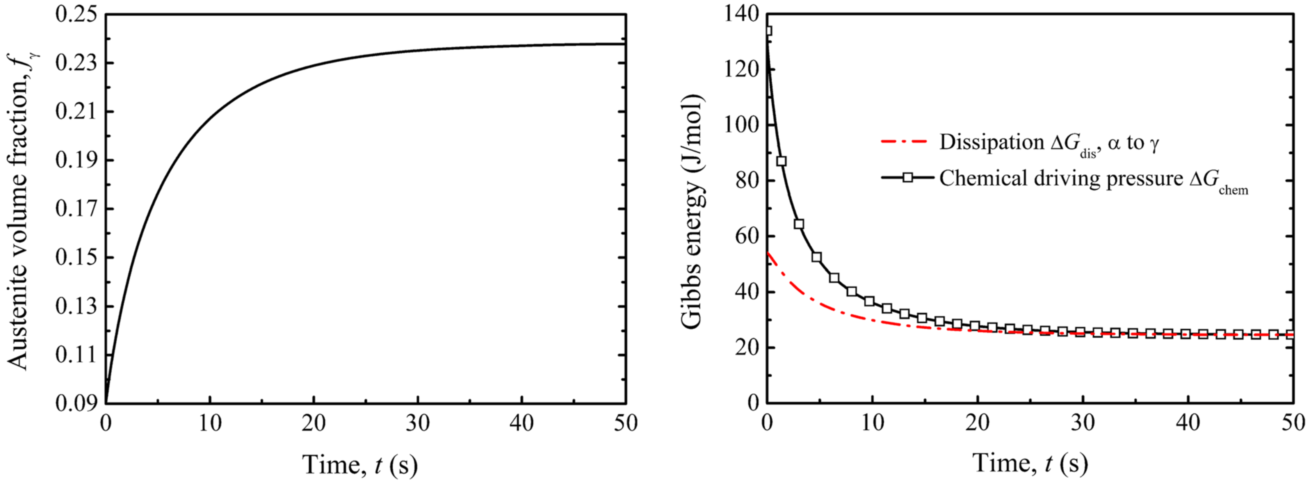

(a) **(b)**

Fig. 7—Simulated (*a*) γ-volume fraction (f_γ) and (*b*) chemical driving pressure and dissipation as a function of time during isothermal holding at 800 °C for 300 s.

since the interfacial carbon concentration of the γ-phase decreases as the $\alpha \rightarrow \gamma$ transformation proceeds. The calculated ΔG_{dis} also decreases gradually with time. After ~ 20 seconds, ΔG_{chem} and ΔG_{dis} become close, leading to the interfacial velocity decreasing. After around 40 seconds, the $\alpha \rightarrow \gamma$ transformation is nearly stopped even though ΔG_{chem} is still larger than zero. This explains why the $\alpha \rightarrow \gamma$ transformation cannot reach the paraequilibrium state with the existence of Gibbs energy dissipation, Figures 6 and 7(a). This result is coincident with the PF simulation by Chen *et al.*[30]

C. *Continuous Cooling Process*

The simulation of continuous cooling is performed from 800 °C to room temperature at a cooling rate of 6 °C s^{-1}. The microstructure and carbon distribution of Figure 6(d) are taken as the initial condition. As described in Section III–D, when the temperature is higher than the M_s temperature, the $\gamma \rightarrow \alpha$ transformation occurs accompanied by the redistribution of carbon. When cooled down to the M_s temperature, the remaining γ-phase instantaneously transforms to martensite. Since the cooling time from the M_s temperature to room temperature is only about 15 seconds, the root-mean square diffusion distance of carbon ($\sqrt{4Dt}$), 1.06×10^{-4} μm, is much smaller than the CA grid spacing of 0.3 μm. Therefore, carbon diffusion below the M_s temperature is neglected and the microstructure and carbon distribution at the M_s temperature are taken for those at room temperature.

Figure 8 displays the evolution of simulated microstructure and carbon concentration field during cooling from 800 °C to the M_s temperature (117 °C) at 6 °C s^{-1}. As shown, the simulated microstructure at room temperature (Figure 8(d)) compares reasonably well with the SEM micrograph of the 800AC sample (Figure 2(c)). The martensite volume fraction in Figure 8(d) is 0.065, which is nearly identical with the value, ~ 0.064, experimentally measured from the 800AC sample. It can be seen that the carbon concentrations in both the α- and γ-phases increase and gradually become non-uniform as the $\gamma \rightarrow \alpha$ transformation progresses. However, the carbon concentrations in γ-grains change little when the temperature is below 450 °C (Figures 8(c) and (d)), indicating that the carbon enrichment in martensite mainly forms during the $\gamma \rightarrow \alpha$ transformation from 800 °C to 450 °C. The simulated average carbon concentration in the α-matrix in Figure 8(d) is around 0.059 mol pct. It is observed that small γ-grains exhibit a relatively higher concentration compared to that in larger γ-grains. Small γ-grains have a larger specific surface area, $S_{v,\gamma}$ (the γ/α interfacial area per unit volume of γ-grain). Since the $\gamma \rightarrow \alpha$ transformation occurs at the γ/α interface by rejecting carbon atoms from the newly formed α-phase into the γ-grains, a larger $S_{v,\gamma}$ will generate a higher carbon enrichment in the small γ-grains. As stated in Section II–B, the

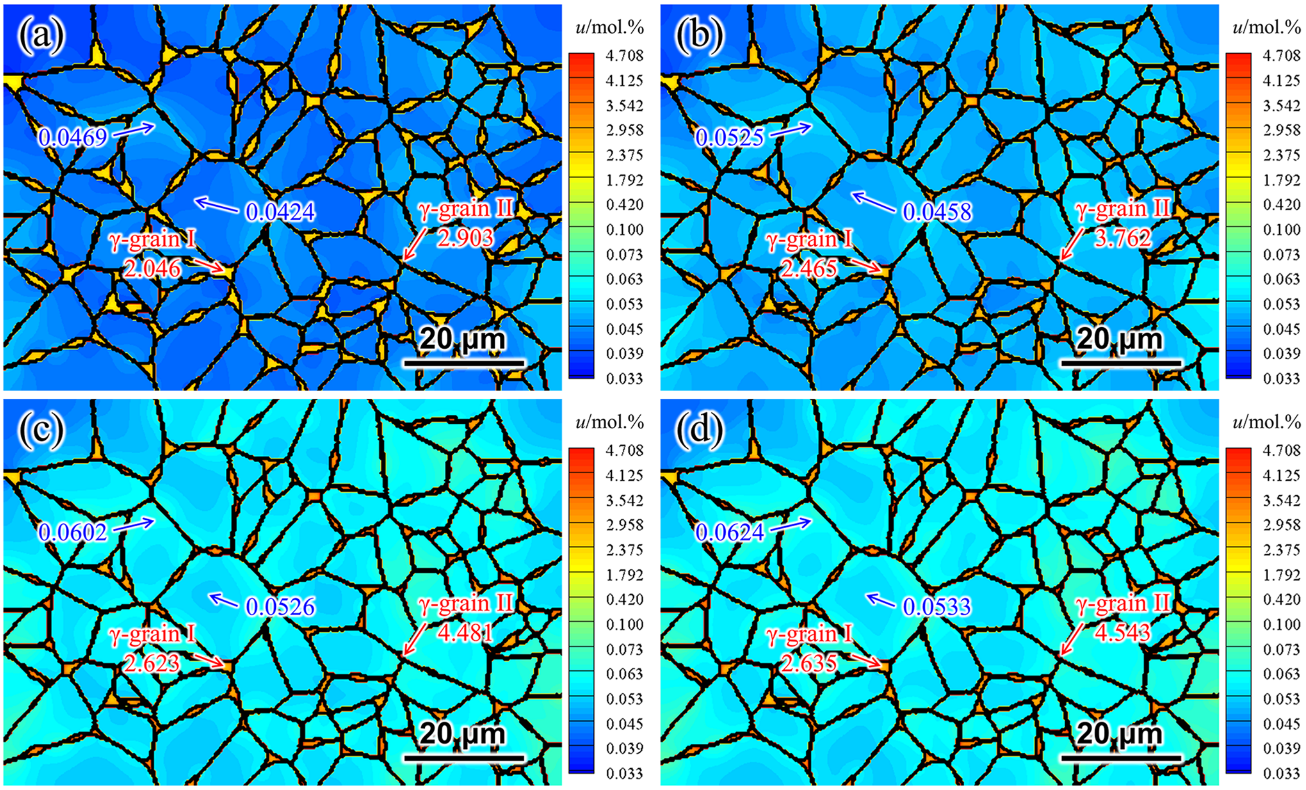

Fig. 8—Simulated microstructures and carbon concentration fields of a Fe-0.323C-1.231Mn-0.849Si (mol pct) alloy after isothermal holding at 800 °C for 300 s and then cooling at 6 °C s^{-1} to the following temperatures: (*a*) 600 °C; (*b*) 550 °C; (*c*) 450 °C; (*d*) 117 °C (taken as the microstructure at room temperature). The numbers in blue and red indicate the local carbon concentrations in the α- and γ-grains, respectively (Color figure online).

martensite in the 800AC sample exhibits different morphologies ranging from lath to fine twins, which can be reasonably explained by the above simulation result that the γ-grains with different sizes have different carbon enrichments.

Figure 9(a) illustrates the normalized γ-volume fractions as a function of time (and temperature) for the overall γ-phase and two γ-grains of different sizes (Grains I and II are the relatively large and small grains, respectively), taken from the simulation of Figure 8. Note that the three curves exhibit the same trend, stationary at the beginning of cooling (the stagnant stage), dropping rapidly from unity during 700 °C to 450 °C, and then the decrease gradually slowing down. When the temperature is below 450 °C, the normalized γ-volume fractions are nearly unchanged. According to Eq. [3], the interfacial mobility ($M^{\alpha/\gamma}$) decreases by three orders of magnitude (from 3.36×10^{-10} to 8.48×10^{-13} mol m J^{-1} s^{-1}) when the temperature decreases from 700 °C to 450 °C. Thus, the phenomenon that the kinetics of the $\gamma \rightarrow \alpha$ transformation becomes extremely low below 450 °C can be attributed to the rapid decreasing interfacial mobility. The $\gamma \rightarrow \alpha$ transformation mainly takes place during cooling from 700 °C to 450 °C. Figure 9(a) also indicates that the profiles of large and small γ-grains are higher and lower than that of the average grain size, respectively, implying that the $\gamma \rightarrow \alpha$ kinetics of smaller grains is greater compared to larger grains. Apparently, this is due to smaller γ-grains having a larger value of $S_{v,\gamma}$, as discussed above. Figure 9(b) plots the chemical driving pressure, ΔG_{chem}, and dissipation, ΔG_{dis}, as a function of time (temperature) during cooling within 30 seconds. As shown, when the cooling process begins, the $\alpha \rightarrow \gamma$ transformation still tends to take place, since the interfacial carbon concentration of the γ-phase $x_C^{\gamma,\alpha/\gamma}$ is higher than the paraequilibrium carbon concentration $x_C^{\gamma,e}$, producing a positive ΔG_{chem}. However, because ΔG_{chem} is smaller than ΔG_{dis} of the $\alpha \rightarrow \gamma$ transformation, the effective driving pressure is forced to be zero and the α/γ interface remains stationary. With the temperature decreasing, $x_C^{\gamma,e}$ increases and ΔG_{chem} decreases. When ΔG_{chem} becomes negative and its absolute value keeps increasing, the transformation of $\gamma \rightarrow \alpha$ will take place. Yet, the α/γ interface does not start moving until the magnitude of ΔG_{chem} is greater than ΔG_{dis} of the $\gamma \rightarrow \alpha$ transformation ($|\Delta G_{\mathrm{chem}}| > |\Delta G_{\mathrm{dis}}|$) after around 10 seconds. Hence, it is understandable that why a stagnant stage appears at the beginning of cooling in the period of ~ 10 seconds. This phenomenon is consistent with the stagnant stage during the cyclic α-γ phase transformation, observed by Chen *et al.* from both experiments and PF simulations.[30]

To further study the compositional features of martensite, a CA simulation using a smaller cell size $\Delta x = 0.15\ \mu$m is performed in a domain consisting of a 312×216 grid. The simulated microstructure and carbon concentration field are displayed in Figure 10(a). Carbon concentration gradients in both the α- and γ-phases are clearer in the magnified microstructure. Two martensitic grains are selected to plot the simulated carbon concentration profiles across the α/M interfaces, Figures 10(b) and (c), along the directions indicated by the arrows in Figure 10(a). Both profiles show the feature that the carbon concentration increases from a low value in the α-phase to a high level in the martensite, ~ 3.1 mol pct for profile 1 and ~ 4.5 mol pct for profile 2, which also confirms that the carbon enrichments in different γ-grains are somewhat different. Additionally, both concentration profiles in the martensite region display a slight amount of segregation near the α/M interface, which is caused by the accumulation of rejected carbon atoms at the

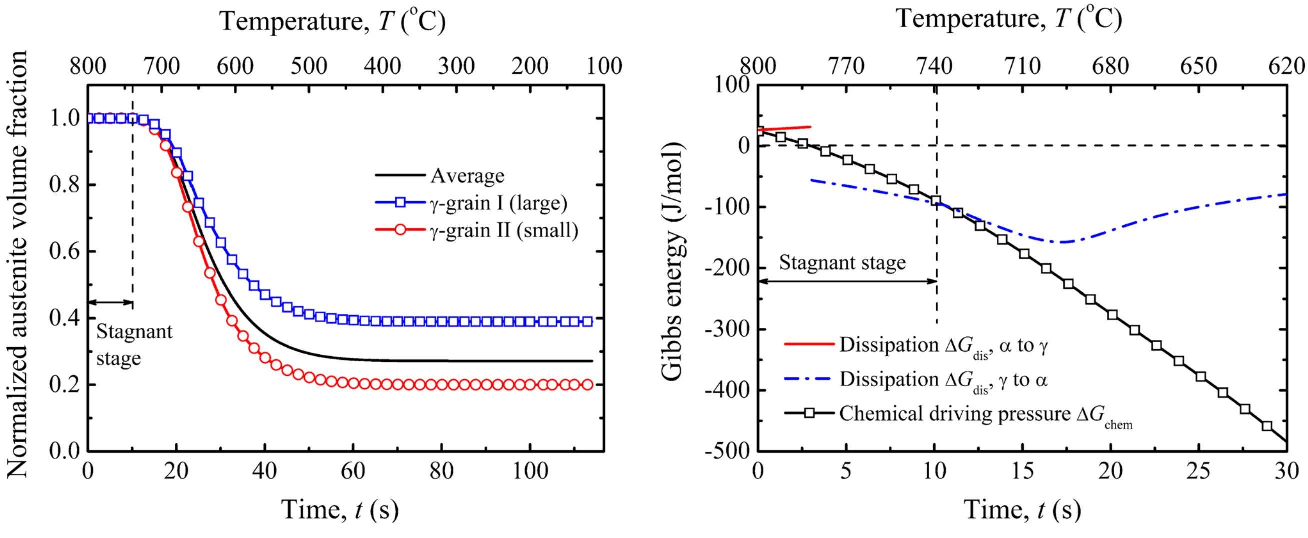

(a) **(b)**

Fig. 9—(*a*) Normalized γ-volume fractions as a function of time (temperature) for overall γ-grains (average) and two γ-grains with different sizes taken from the simulation of Fig. 8; (*b*) chemical driving pressure and dissipation as a function of time (temperature) during cooling at 6 °C s^{-1}.

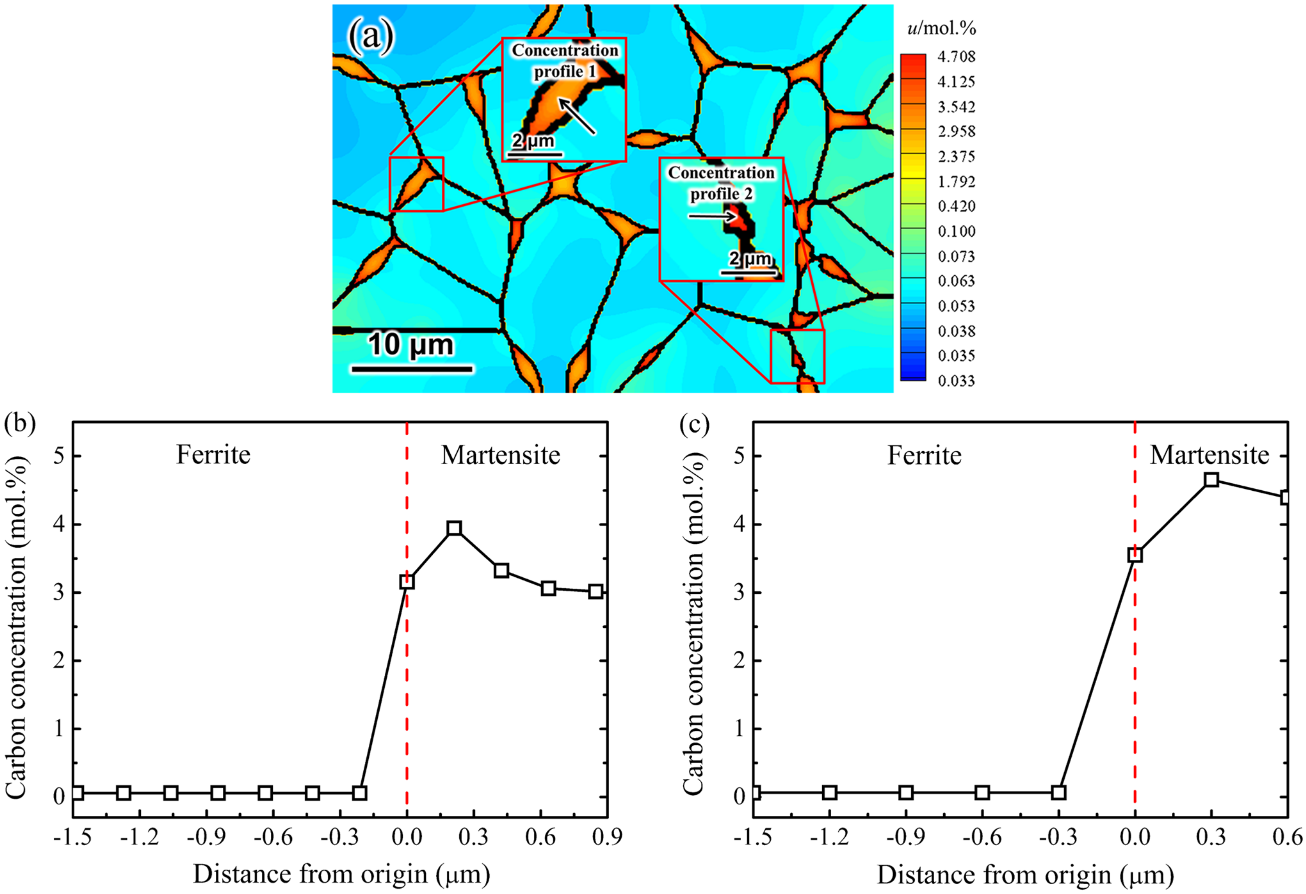

Fig. 10—Simulated microstructure and carbon concentration field of a Fe-0.323C-1.231Mn-0.849Si (mol pct) alloy after isothermal holding at 800 °C for 300 s and then cooling to 117 °C at 6 °C s^{-1}: (*a*) magnified morphology; and (*b*) and (*c*) carbon concentration profiles 1 and 2 across the α/M interfaces for different martensitic grains, along the indicated arrows in (a), respectively (Color figure online).

interface due to the carbon partitioning during the $\gamma \rightarrow \alpha$ transformation. Note that there is also a narrow region enriched in carbon atoms at the α/M interface according to APT measurement (Figure 3(a)), which is considered to be caused by interfacial segregation at the α/M interface.[49,50] Although the length scale of the CA simulation, Figure 10, is larger than that of the APT measurement, the simulated carbon concentration level in martensite compares reasonably well with the APT analyses.

D. *Tempering Process*

During tempering at 400 °C, martensite decomposition is simulated using the time differential of Eq. [11]. The microstructure and carbon distribution of Figure 8(d) are taken as the initial condition. According to the APT analysis of the tempered sample, the carbon concentrations of the α-phase inside the TM are in the range from ~ 0.1 to ~ 0.4 mol pct, while the carbon concentrations of the α-matrix outside the TM are lower than ~ 0.1 mol pct. Thus, carbon concentration gradients ahead of the α/TM interface are established, leading to carbon diffusion from the TM into the α-matrix during tempering. In addition, the simulation of the cooling process indicates that martensite grains with different sizes have different carbon concentrations (see Figures 8 and 10). Therefore, it is estimated that inside the TM-grains the carbon concentration of the α-phase and the volume fraction of carbides range from ~ 0.1 to ~ 0.4 mol pct and from ~ 0.1 to ~ 0.2, respectively, using the lever rule depending on the carbon concentrations of the original martensitic grains. The evolution of the simulated carbon concentration field during tempering is presented in Figure 11. Considering the low volume fraction and small size of the carbides, the TM is displayed as one effective phase using the average carbon concentration of the decomposed α-phase and carbides in each TM-grain. As shown, with tempering time increasing, the overall carbon concentration of the α-matrix increases and the carbon distribution in the α-matrix becomes gradually uniform. After tempering at 400 °C for 20 minutes (Figure 11(b)), the average carbon concentration of the α-matrix, ~ 0.080 mol pct, is higher than that in the simulated air cooled microstructure (Figure 8(d)), ~ 0.059 mol pct. The tempered microstructures obtained by the CA simulation (Figure 11(b)) and metallography (Figure 2(d)) are comparable.

It is noted that the present CA model is computationally efficient. The computational times for simulating isothermal holding (Figure 6), continuous cooling

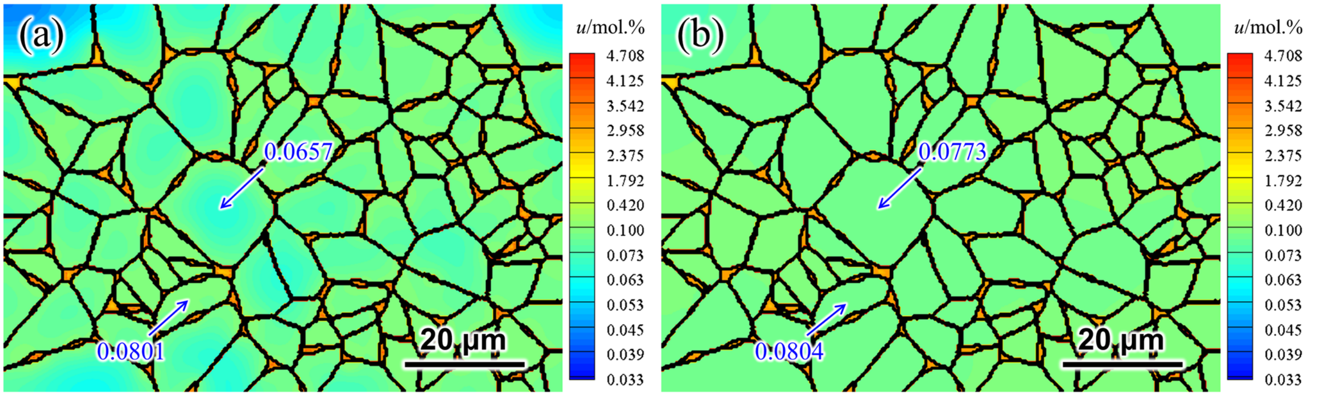

Fig. 11—Simulated microstructures and carbon concentration fields of a Fe-0.323C-1.231Mn-0.849Si (mol pct) alloy after isothermal holding at 800 °C for 300 s, subsequent cooling to room temperature at 6 °C s^{-1} and then tempering at 400 °C for: (*a*) 3 min; (*b*) 20 min. The numbers in the figures indicate the local carbon concentrations in the α-matrix (Color figure online).

(Figure 8) and tempering (Figure 11) are about 5.5, 3.5 and 0.15 hours, respectively, on a PC with Core i5-6500 (3.20 GHz).

E. *Discussion*

As presented in Figure 1 and Table I, the samples before and after different heat treatments exhibit different yield platforms and yield strengths. It is considered that the mechanical properties of the as-rolled sample must be influenced by more factors compared to the heat treated samples due to the complicated rolling process. Besides, in the present work we did not perform the simulation of the rolling process. Thus, in this section we focus on the discussion regarding the samples after heat treatments.

As discussed in Section II, the average α-grain size is nearly unchanged after heat treatments, and the volume fractions of martensite and TM in the 800AC and 800AC-400T samples are less than 0.10, which are not sufficient to influence the yield strength.[37] Therefore, different concentrations of Cottrell atmospheres formed in the α-matrix are considered to be the main reason responsible for the different yield point phenomena of samples after different heat treatments, which is closely related to the carbon concentration in the α-matrix.[38,39]

Recently, evidence of Cottrell atmospheres was found in modeled alloys or specimens such as Si with As dopant after implantation[51] and Mn partitioning to dislocation cores in a Fe-9 wt pct Mn steel.[52] However, there are still limitations for the detection of carbon segregations at dislocation cores, because carbon is a fast diffuser in the α-matrix and can also be easily moved by applied bias in the LEAP, especially under an increased surface temperature with laser pulse assisted field evaporation. Additionally, the carbon concentrations in the current steel are extremely low in the matrix. It is thus difficult to obtain precise carbon concentrations in the α-matrix and find clear evidence of Cottrell atmospheres in current APT experiments.

According to the simulation results presented in Sections IV–B through IV–D, martensitic grains enriched in carbon (~ 3 to ~ 5 mol pct) form after holding at 800 °C for 300 seconds, and then cooling at 6 °C s^{-1} to the M_s temperature. Such carbon enrichment in martensite reduces the amount of carbon in solution in the α-matrix. The simulated average carbon concentration in the α-matrix is about 0.059 mol pct, Figure 8(d).

During tempering, martensite decomposes into TM and releases carbon atoms into the α-matrix. According to the CA simulation, after tempering the overall carbon concentration in the α-matrix increases from ~ 0.059 to ~ 0.080 mol pct, compared to the 800AC sample. Apparently, the increased carbon concentration in the α-matrix and sufficient carbon diffusion during tempering render the formation of more Cottrell atmospheres. Thus, it is expected that the possibility of dislocations pinned by Cottrell atmospheres is markedly increased with more carbon in solution. In other words, the formation of Cottrell atmospheres surrounding dislocations is promoted after tempering, which contributes to the strain aging effect of the α-matrix, leading to a clear and long yield platform in the stress–strain curve, and a concomitant increased yield strength.[38,39] Accordingly, it is understandable that the tempered sample, 800AC-400T, presents a longer yield platform and a higher yield strength than those of the air cooled sample, 800AC, Figure 1 and Table I.

V. CONCLUSIONS

A 2-D CA model is proposed and applied to simulate the evolution of microstructure and carbon distribution during phase transformations occurring in a Fe-0.323C-1.231Mn-0.849Si (mol pct) steel subject to different heat treatments. Model validation is performed by comparing the CA simulations with the PF predictions[30] with and without considering Gibbs energy dissipation for the transformation kinetics during isothermal holding at the inter-critical temperature of 785 °C for a Fe-C-Mn ternary alloy. Good agreement is obtained between the results of the two models. The CA simulated microstructures and carbon content of martensite agree reasonably well with the SEM micrographs and APT analyses, respectively. The following conclusions are reached:

- During isothermal holding at 800 °C, the growth of pearlite-nucleated γ-grains consumes the supersaturated carbon atoms in the γ-phase, while the growth of γ-nuclei formed at α/α GBs absorbs the carbon atoms from the adjacent α-phase. The carbon concentrations in both the α- and γ-phases decrease and become uniform gradually as the $\alpha \rightarrow \gamma$ transformation proceeds. After holding for 300 seconds, the carbon concentrations in the α- and γ-phases, as well as the transformed volume fraction of the γ-phase, still deviate from the paraequilibrium predictions, due to the existence of Gibbs energy dissipation.
- During cooling from 800 °C to room temperature at 6 °C s^{-1}, after a stagnant stage at the beginning, the $\gamma \rightarrow \alpha$ transformation takes place, accompanied by the carbon concentrations in the α- and γ-phases increasing and becoming non-uniform. Small γ-grains have faster transformation kinetics and higher carbon concentrations compared to large γ-grains, which explains the reason why different martensitic substructures are observed in the 800AC sample. The transformation kinetics becomes extremely low below 450 °C due to the rapidly decreasing interfacial mobility. When cooled to the martensite start (M_s) temperature, there is ~ 0.065 volume fraction of the γ-phase remaining, which transforms to martensitic grains and the quantity is nearly identical with the martensite volume fraction experimentally measured from the 800AC sample. The simulated concentration profiles across the α/M interfaces reveal the enrichment of carbon atoms (~ 3 to ~ 5 mol pct) in martensite, which compares well with the results of APT analyses. During subsequent tempering at 400 °C for 20 minutes, martensite decomposition and carbon diffusion occur, leading to the increasing carbon concentration in the α-matrix. The simulated average carbon concentration in the α-matrix of the tempered microstructure is higher than that of the air cooled microstructure.
- According to the simulation results, a small volume fraction of carbon enriched martensite exists in the microstructure of the air cooled sample, which reduces the amount of carbon atoms in solution in the α-matrix. During tempering, martensite decomposition releases carbon atoms into the α-matrix and carbon diffusion in the α-matrix is promoted. With more carbon atoms in solution, high concentration Cottrell atmospheres are expected to form around dislocations, leading to a clear yield platform and a high yield strength. Consequently, the CA simulations provide insights into the interaction of microstructure evolution and carbon distribution, and the mechanisms of the experimental phenomena that the tempered sample exhibits a more distinct yield platform and a higher yield strength compared to the air cooled sample.

ACKNOWLEDGMENTS

This work was financially supported by A. O. Smith Corporation, USA, NSFC (Grant Nos. 51371051, 51501091), the Jiangsu Key Laboratory for Advanced Metallic Materials (BM2007204), and the Scientific Research Foundation of Graduate School of Southeast University (YBJJ1628). Mr. Dong An is grateful for the financial support from the China Scholarship Council (CSC). APT was performed at the Northwestern University Center for Atom-Probe Tomography (NUCAPT). The LEAP tomograph at NUCAPT was purchased and upgraded with Grants from the NSF-MRI (DMR-0420532) and ONR-DURIP (N00014-0400798, N00014-0610539, N00014-0910781, N00014-1712870) Programs. This work made use of the EPIC Facility of Northwestern University's NUANCE Center. NUCAPT and NUANCE received support through the MRSEC Program (NSF DMR-1720139) at the Materials Research Center and the SHyNE Resource (NSF ECCS-1542205), NUCAPT from the Initiative for Sustainability and Energy (ISEN), at Northwestern University; NUANCE from the International Institute for Nanotechnology (IIN); the Keck Foundation; and the State of Illinois, through the IIN.

REFERENCES

1. M. Gouné, F. Danoix, J. Ågren, Y. Bréchet, C.R. Hutchinson, M. Militzer, G. Purdy, S. van der Zwaag, and H. Zurob: *Mater. Sci. Eng. R*, 2015, vol. 92, pp. 1–38.
2. C.C. Tasan, M. Diehl, D. Yan, M. Bechtold, F. Roters, L. Schemmann, C. Zheng, N. Peranio, D. Ponge, M. Koyama, K. Tsuzaki, and D. Raabe: *Annu. Rev. Mater. Res.*, 2015, vol. 45, pp. 391–431.
3. G. Krauss: *Steels: Processing, Structure, and Performance*, 2nd ed., ASM International, Materials Park, OH, 2015.
4. J. Sietsma and S. van der Zwaag: *Acta Mater.*, 2004, vol. 52, pp. 4143–52.
5. C. Bos and J. Sietsma: *Scripta Mater.*, 2007, vol. 57, pp. 1085–88.
6. M.G. Mecozzi, C. Bos, and J. Sietsma: *Acta Mater.*, 2015, vol. 88, pp. 302–13.
7. A. Hultgren: *Trans. ASM*, 1947, vol. 39, pp. 915–1005.
8. G.R. Purdy and Y.J.M. Brechet: *Acta Metall. Mater.*, 1995, vol. 43, pp. 3763–74.
9. H. Chen and S. van der Zwaag: *Acta Mater.*, 2014, vol. 72, pp. 1–12.
10. Z.Q. Liu, G. Miyamoto, Z.G. Yang, and T. Furuhara: *Acta Mater.*, 2013, vol. 61, pp. 3120–29.
11. Y. Kubo, K. Hamada, and A. Urano: *Ultramicroscopy*, 2013, vol. 135, pp. 64–70.
12. T.F. Kelly and M.K. Miller: *Rev. Sci. Instrum.*, 2007, vol. 78, p. 031101.
13. D.N. Seidman: *Annu. Rev. Mater. Res.*, 2007, vol. 37, pp. 127–58.
14. Y.R. Wen, Y.P. Li, A. Hirata, Y. Zhang, T. Fujita, T. Furuhara, C.T. Liu, A. Chiba, and M.W. Chen: *Acta Mater.*, 2013, vol. 61, pp. 7726–40.
15. Y. Toji, H. Matsuda, M. Herbig, P.-P. Choi, and D. Raabe: *Acta Mater.*, 2014, vol. 65, pp. 215–28.
16. M.I. Hartshorne, D. Isheim, D.N. Seidman, and M.L. Taheri: *Ultramicroscopy*, 2014, vol. 147, pp. 25–32.
17. S.-I. Baik, L. Ma, Y.-J. Kim, B. Li, M. Liu, D. Isheim, B.I. Yakobson, P.M. Ajayan, and D.N. Seidman: *Small*, 2015, vol. 11, pp. 5968–74.
18. J. Rudnizki, B. Böttger, U. Prahl, and W. Bleck: *Metall. Mater. Trans. A*, 2011, vol. 42A, pp. 2516–25.
19. C. Zheng and D. Raabe: *Acta Mater.*, 2013, vol. 61, pp. 5504–17.

20. B. Su, Z. Han, and B. Liu: *ISIJ Int*., 2013, vol. 53, pp. 527–34.
21. B. Zhu, Y. Zhang, C. Wang, P.X. Liu, W.K. Liang, and J. Li: *Metall. Mater. Trans. A*, 2014, vol. 45A, pp. 3161–71.
22. G. Zhu, Y. Kang, C. Lu, and S. Li: *Steel Res. Int*., 2014, vol. 85, pp. 1035–46.
23. M. Militzer, M.G. Mecozzi, J. Sietsma, and S. van der Zwaag: *Acta Mater*., 2006, vol. 54, pp. 3961–72.
24. D.Z. Li, N.M. Xiao, Y.J. Lan, C.W. Zheng, and Y.Y. Li: *Acta Mater*., 2007, vol. 55, pp. 6234–49.
25. D.S. Svyetlichnyy and A.I. Mikhalyov: *ISIJ Int*., 2014, vol. 54, pp. 1386–95.
26. B. Su, Q. Ma, and Z. Han: *Steel Res. Int*., 2017, vol. 88, p. 1600490.
27. C. Bos, M.G. Mecozzi, and J. Sietsma: *Comput. Mater. Sci*., 2010, vol. 48, pp. 692–99.
28. B. Zhu and M. Militzer: *Metall. Mater. Trans. A*, 2015, vol. 46A, pp. 1073–84.
29. B. Zhu, H. Chen, and M. Militzer: *Comput. Mater. Sci*., 2015, vol. 108, pp. 333–41.
30. H. Chen, B. Zhu, and M. Militzer: *Metall. Mater. Trans. A*, 2016, vol. 47A, pp. 3873–81.
31. D. An, S. Pan, L. Huang, T. Dai, B. Krakauer, and M. Zhu: *ISIJ Int*., 2014, vol. 54, pp. 422–29.
32. *Image Tool Program*. University of Texas Health Science Center, San Antonio, 2002. http://compdent.uthscsa.edu/dig/itdesc.html. Accessed 05 March 2018.
33. G. Krauss: *Mater. Sci. Eng. A*, 1999, vols. 273–275, pp. 40–57.
34. G.R. Speich and W.C. Leslie: *Metall. Trans*., 1972, vol. 3, pp. 1043–54.
35. G.F. Vander Voort: *Atlas of Time–Temperature Diagrams for Irons and Steels*, ASM International, Materials Park, OH, 1991.
36. O.C. Hellman, J.A. Vandenbroucke, J. Rüsing, D. Isheim, and D.N. Seidman: *Microsc. Microanal*., 2000, vol. 6, pp. 437–44.
37. P.H. Chang and A.G. Preban: *Acta Metall*., 1985, vol. 33, pp. 897–903.
38. A.H. Cottrell and B.A. Bilby: *Proc. Phys. Soc. A*, 1949, vol. 62, pp. 49–62.
39. E.O. Hall: *Yield Point Phenomena in Metals and Alloys*, Springer US, Boston, 1970.
40. R. Rementeria, J.D. Poplawsky, M.M. Aranda, W. Guo, J.A. Jimenez, C. Garcia-Mateo, and F.G. Caballero: *Acta Mater*., 2017, vol. 125, pp. 359–68.
41. V.I. Savran, S.E. Offerman, and J. Sietsma: *Metall. Mater. Trans. A*, 2010, vol. 41A, pp. 583–91.
42. G.S. Huppi, D.K. Matlock, and G. Krauss: *Scripta Metall*., 1980, vol. 14, pp. 1239–43.
43. G.P. Krielaart and S. Van Der Zwaag: *Mater. Sci. Technol*., 1998, vol. 14, pp. 10–18.
44. F. Fazeli and M. Militzer: *Metall. Mater. Trans. A*, 2005, vol. 36A, pp. 1395–1405.
45. J.R. Bradley and H.I. Aaronson: *Metall. Trans. A*, 1977, vol. 8, pp. 317–22.
46. C. Capdevila, F.G. Caballero, and C.G. de Andrés: *ISIJ Int*., 2002, vol. 42, pp. 894–902.
47. L. Cheng, C.M. Brakman, B.M. Korevaar, and E.J. Mittemeijer: *Metall. Trans. A*, 1988, vol. 19, pp. 2415–26.
48. T. Waterschoot, K. Verbeken, and B.C. De Cooman: *ISIJ Int*., 2006, vol. 46, pp. 138–46.
49. D. Isheim, A.H. Hunter, X.J. Zhang, and D.N. Seidman: *Metall. Mater. Trans. A*, 2013, vol. 44A, pp. 3046–59.
50. D. Jain, D. Isheim, X.J. Zhang, G. Ghosh, and D.N. Seidman: *Metall. Mater. Trans. A*, 2017, vol. 48A, pp. 3642–54.
51. K. Thompson, P.L. Flaitz, P. Ronsheim, D.J. Larson, and T.F. Kelly: *Science*, 2007, vol. 317, pp. 1370–74.
52. A. Kwiatkowski da Silva, G. Leyson, M. Kuzmina, D. Ponge, M. Herbig, S. Sandlöbes, B. Gault, J. Neugebauer, and D. Raabe: *Acta Mater*., 2017, vol. 124, pp. 305–15.